Scaling Law for Marginal Ignition

Introduction

In recent years, a considerable effort[1–6] has been made to determine the minimum energy required for ignition in inertial confinement fusion (ICF) implosions. Though different conclusions have been reached by different authors, consensus is that the minimum energy required for ignition is a strong function of the shell implosion velocity as well as the shell adiabat. Various approaches to the study of ignition have led to scaling laws in which the shell kinetic energy required for ignition is given as a function of the implosion velocity, shell adiabat (in-flight and at stagnation), and other parameters such as the applied pressure at the end of the acceleration phase. Scientists from Lawrence Livermore National Laboratory (LLNL) have produced a scaling law[1,5] for marginal ignition by fitting a large database of *LASNEX* simulations of implosions with gain approximately equal to unity. The first scaling law by Levedahl and Lindl (LL)[1] was obtained by fitting the shell kinetic energy with the in-flight shell adiabat and the shell implosion velocity. The LL scaling law yields

$$E_k \sim \frac{\beta_{\mathrm{if}}^{1.7}}{V_{\mathrm{imp}}^{5.5}}, \qquad (1)$$

where E_k is the shell kinetic energy at the end of the acceleration phase, β_{if} is the in-flight shell adiabat, and V_{imp} is the shell implosion velocity. In the derivation of Eq. (1), the different hydrodynamic quantities have been rescaled by keeping the initial pressure constant. A similar result was also obtained by Piriz.[2] Later, Basko and Johner (BJ) derived a similar scaling law[4] from a set of numerical simulations based on a self-similar rescaling of the hydrodynamic quantities. Their conclusion is that the minimum energy required for ignition scales as

$$E_k \sim \frac{\beta_{\mathrm{if}}^{3}}{V_{\mathrm{imp}}^{9.1}}. \qquad (2)$$

At first glance, the BJ scaling appears quite different from the LL scaling; however, it must be emphasized that the hydrodynamic similarity used by Basko and Johner requires that the pressure scales as $P \sim V_{\mathrm{imp}}^{5}\beta_{\mathrm{if}}^{-1.5}$ in contrast with the $P \sim$ *constant* assumption used in the derivation of the LL scaling. Relations (1) and (2) seem at odds with the standard static assembled scaling based on the isobaric model of Meyer-ter-Vehn,[7]

$$E_k \sim \frac{J_s^{3}\beta_s^{3}}{V_{\mathrm{imp}}^{10}}, \qquad (3)$$

where β_s is the stagnation adiabat and $J_s \equiv \rho_s R_s T_s$ with ρ_s, R_s, and T_s representing the hot-spot density, radius, and temperature at stagnation.

It is important to emphasize that the shell adiabat used in Eq. (3) is calculated at stagnation and its value differs from the in-flight adiabat used in Eqs. (1) and (2). This point was not made by Basko and Johner, who did not distinguish between the in-flight and stagnation adiabats. It follows that a comparison between Eq. (3) and Eqs. (1) and (2) cannot be made unless a relation between the in-flight and stagnation adiabats is derived. Thus Eq. (3) and Eqs. (1) and (2) represent two different scalings that we denote as the "stagnation" scaling and "in-flight" scaling, respectively.

Another important point concerning the ignition condition is the following: If ignition is triggered at a fixed value of J_s (as commonly assumed), Eq. (3) yields a stagnation scaling

$$E_k \sim \frac{\beta_s^{3}}{V_{\mathrm{imp}}^{10}}. \qquad (4)$$

This result disagrees with the stagnation scaling recently found by Herrmann, Tabak, and Lindl (HTL)[5] based on a numerical fit of *LASNEX* runs leading to

$$E_k \sim \frac{\beta_s^{2.66}}{V_{\text{imp}}^{7.2}}. \qquad (5)$$

Basko and Johner[4] pointed out that the condition $J_s = constant$ does not correctly represent the ignition conditions because it neglects the tamping effect of the shell. This is important because the shell's inertia determines the hot-spot disassembly time. Basko and Johner estimated analytically that, at ignition, J_s depends linearly on the implosion velocity $J_s \sim V_{\text{imp}}$, thus leading to the modified ignition scaling [from Eq. (3)]

$$E_k \sim \frac{\beta_s^3}{V_{\text{imp}}^7}. \qquad (6)$$

Basko and Johner revised this scaling[4] through a set of numerical simulations starting from the assembled state and derived what they define as the "dynamic assembled state scaling"

$$(7)$$

With the exception of minor differences in the exponents, all the stagnation scalings [Eqs. (5)–(7)] seem to agree and corroborate the argument that J_s is proportional to the implosion velocity or to some power (<1) of it.

Herrmann *et al.*[5] revised the in-flight scaling of Levedahl and Lindl through a series of *LASNEX* simulations, allowing for changes in the shell pressure at the end of the acceleration phase, and concluded that the energy scaling in terms of the in-flight variables can be approximated by the following fit:

$$E_k \sim \frac{\beta_{\text{if}}^{1.8}}{V_{\text{imp}}^{5.8} P_a^{0.77}}, \qquad (8)$$

where P_a is the applied pressure at the end of the acceleration phase (i.e., at the peak of the shell kinetic energy). It is important to notice that the in-flight HTL scaling [Eq. (8)] reproduces the in-flight BJ scaling [Eq. (2)] when the self-similar hydrodynamic scaling for the pressure $P \sim V_{\text{imp}}^5 / \beta_{\text{if}}^{3/2}$ is substituted into Eq. (8). Recently, Kemp, Meyer-ter-Vehn, and Atzeni (KMA)[6] analytically reproduced a scaling law that resembles the in-flight HTL scaling [Eq. (8)]:

$$E_k \sim J_s^3 \frac{\beta_{\text{if}}^{1.8}}{V_0^6 P_0^{0.8}}. \qquad (9)$$

Equation (9) was derived from a self-similar solution of an imploding shell where P_0 and V_0 are the peak pressure and velocity at the time of void closure. Even though it is unclear how to relate P_0 in Eq. (9) to P_a in the HTL scaling [Eq. (8)], the two scaling laws are strikingly similar if J_s is constant at the onset of ignition. However, if J_s scales linearly with the implosion velocity as suggested by Basko,[3] the KMA scaling will produce a weak dependence on the implosion velocity and significantly deviate from the HTL scaling. Another important conclusion of the KMA self-similar solution is that the stagnation adiabat is related to its in-flight value through the shell Mach number:

$$\beta_s \sim \beta_{\text{if}} \sqrt{M_A} \sim \beta_{\text{if}}^{0.85} V_{\text{imp}}^{0.5} P_0^{-0.1}, \qquad (10)$$

where M_A is the shell Mach number. A similar scaling between the adiabats was also derived in Ref. 5 through a fit of the *LASNEX* simulation database, yielding

$$\beta_s \sim \beta_{\text{if}}^{0.75} V_{\text{imp}}^{0.44} P_a^{-0.21}. \qquad (11)$$

Observe that the HTL scaling [Eq. (8)] can also be approximately derived from the stagnation scaling [Eqs. (5)–(7)] by using Eq. (11) to relate the stagnation and in-flight adiabats.

Though many discrepancies have been resolved with regard to the different scalings, it is important to note that some differences persist. In particular, the analytic KMA scaling [Eq. (9)] reproduces the in-flight HTL scaling [Eq. (8)] only if J_s is independent of the implosion velocity. On the other hand, the stagnation scaling in Eq. (3) reproduces the stagnation HTL scaling [Eq. (5)] only if $J_s \sim V_{\text{imp}}$, as proposed by Basko and Johner. This leads to the paradox that the two analytic theories leading to Eqs. (3) and (6) and Eq. (9) match the numerical fits only when different ignition conditions are used ($J_s = constant$ or $J_s \sim V_{\text{imp}}$).

In this article, a new model is developed to determine the marginal ignition conditions and the minimum kinetic energy required for ignition. This model includes the propagation of the return shock through the shell and the change of the shell adiabat as well as the most-relevant ignition physics such as alpha-particle heating and heat-conduction losses. It repro-

duces BJ scaling and HTL scaling with respect to the stagnation adiabat, indicating that J_s is indeed proportional to the implosion velocity. Furthermore, the model yields a relation between the stagnation and in-flight adiabats that is in general agreement with the KMA scaling and the HTL scaling [Eqs. (10) and (11)].

The following sections of this article (1) describe hot-spot dynamics and shell dynamics; (2) derive the ignition scalings with respect to the stagnation adiabat; (3) relate the stagnation adiabat to the in-flight adiabat and derive the "in-flight" scaling; and (4) verify *a posteriori* all the assumptions concerning the hot-spot hydrodynamics.

Hot-Spot Dynamics

The hot spot is a low-density plasma heated by the shock and by the *PdV* work of the cold, dense surrounding shell. It is made of ionized DT gas and the plasma ablated off the inner shell surface. Its dynamics are determined by the compression of the shell, the energy conduction and radiation losses, and the alpha heating.

As the hot spot is formed after the shock reflection, its temperature is typically large enough that its sound speed is larger than the flow velocity. Therefore, it is a good approximation to neglect the hot-spot kinetic energy with respect to its internal energy throughout the assembly and ignition stages of the hot spot. Another consequence of the subsonic flow assumption is that the pressure is equilibrated and the pressure profile is flat within the hot spot, i.e., $P_{hs} \simeq P_{hs}(t)$.

Bremsstrahlung radiation energy losses can also be neglected because their contribution is typically smaller than that of the mechanical work and/or the fusion power. The magnitude of the radiation losses is larger than the fusion power for temperatures below 4.4 keV, when the *PdV* work rate is typically greater than both radiation and fusion power. Thus, at such low temperatures, both radiation losses and alpha heating power are negligible with respect to the compression work rate. The *PdV* work rate decreases as the shell approaches the stagnation point, while higher temperatures are reached within the hot spot. If these temperatures are well above 4.4 keV, the alpha power is greater than the radiation losses and the bremsstrahlung term can again be neglected in the energy equation.

Another simplification is the assumption that the alpha particles are locally deposited. This approximation requires a condition on the hot-spot temperature and areal density that can be satisfied for sufficiently large implosion velocities. Indeed, it will be shown *a posteriori* [Eq. (10)] that both bremsstrahlung radiation and alpha-particle diffusion can be neglected as long as the implosion velocity is larger than a critical value.

Based on previous assumptions, the energy conservation equation for the hot spot includes the *PdV* work of the shell, the conduction energy losses, the alpha-particle heating, and the change in internal energy:

$$\frac{3}{2}\frac{\partial}{\partial t}P + \nabla \cdot \left[\frac{5}{2}\mathbf{v}P\right] = \nabla \cdot \kappa(T)\nabla T + \frac{\rho^2}{4M_i^2}E_\alpha\langle\sigma v\rangle, \quad (12)$$

where ρ is the hot-spot density, M_i is the ion mass, $E_\alpha \simeq$ 3.5 MeV is the alpha-particle energy, $\kappa(T) \simeq \kappa_0 T^{5/2}$ is Spitzer thermal conductivity, and $P \simeq P_{hs}(t)$ for subsonic flows.

Following Ref. 8, we integrate Eq. (12) over the hot-spot volume enclosed by the inner shell surface and approximate the fusion cross section with the quadratic form $\langle\sigma v\rangle \simeq S_\alpha T^2$ with $S_\alpha \simeq 10^{-18}$ cm^{3}s^{-1} keV^{-2}. Figure 87.46 shows that the error produced by the T^2 approximation of $\langle\sigma v\rangle$ is less than 30% for $6 < T < 25$ keV. At the inner surface, the shell material is cold and the thermal conduction can be neglected. This leads to the following form of the integrated energy equation:

$$\frac{d}{dt}\left(P_{hs}R_{hs}^3\right) + 3R_{hs}^2 P_{hs}\left[\frac{5}{3}U(R_{hs},t) - \frac{dR_{hs}}{dt}\right]$$

$$= \Sigma_\alpha P_{hs}^2 R_{hs}^3, \quad (13)$$

where $U(R_{hs},t)$ is the flow velocity at the shell inner surface and $\Sigma_\alpha \equiv E_\alpha S_\alpha/24$. The flow velocity results from the combination of the inner surface motion and the ablative flow, $U(R_{hs},t) = \dot{R}_{hs} - V_a$, where V_a is the ablation velocity and $\dot{R}_{hs}$ scales with the implosion velocity. Since $V_a \ll \dot{R}_{hs}$, the ablation velocity[8] can be neglected and Eq. (13) can be rewritten in the simplified form

$$\dot{P}_{hs} + 5P_{hs}\frac{\dot{R}_{hs}}{R_{hs}} = \Sigma_\alpha P_{hs}^2. \quad (14)$$
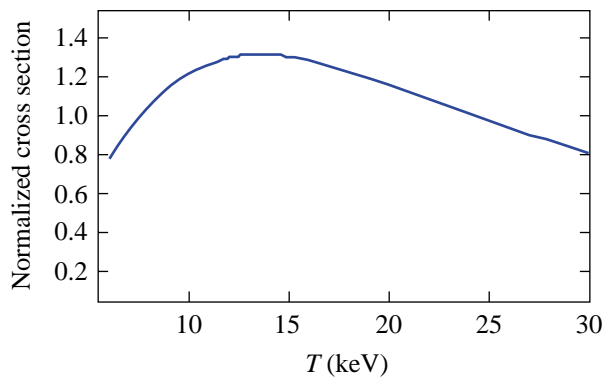
TC5707

Figure 87.46
Plot of the normalized fusion cross section $\langle\sigma v\rangle/0.97 \times 10^{-18}$ T (keV)^2 between 6 and 30 keV. The maximum error is 27%. (The reference cross section is taken from Ref. 9.)

Note that the heat conduction losses do not enter into the global energy balance of the hot spot because the heat flux leaving the hot spot is deposited onto the inner shell surface. A fraction of this energy is transformed into internal energy of the shell material ablating into the hot spot. The remaining fraction produces the PdV work done by the ablated plasma entering the hot spot against the hot-spot pressure. In other words, the energy leaving the hot spot in the form of heat conduction losses goes back into the hot spot in the form of internal energy and compression work of the ablated plasma. Therefore, conduction losses do not affect the global energy balance of the hot spot and therefore do not represent net energy losses to the hot spot, as shown by Eq. (14). It is important to emphasize that the hot-spot energy is proportional to its pressure. The conduction losses do affect the hot-spot temperature but not its pressure. This conclusion implies that greater conduction losses would lower the temperature and raise the density (through larger ablation at the shell inner surface), leaving the pressure ($P \sim \rho T$) unaltered.

The next step is to couple the hot-spot-energy equation [Eq. (14)] with the shell dynamics through the shell momentum conservation and to determine the hot-spot radius as a function of the hot-spot pressure.

Shell Dynamics

In the initial stage of the deceleration phase, the hot spot is heated and compressed by the piston action of the shell. If a sufficiently large pressure is reached within the hot spot, a thermal instability is driven by the absorbed fusion power, leading to a rapid increase of the hot-spot energy. This instabil-

ity is referred to as "thermonuclear ignition." In this section, we develop a simple model describing the shell motion and combine the shell and hot-spot equations in order to construct a self-consistent model of the deceleration phase and hot-spot ignition.

As mentioned in Ref. 8, the deceleration phase starts after the shock reflected from the center of the capsule interacts with the incoming shell. For simplicity, we assume that after the first shock reflects off the shell, all subsequent shocks are weak and do not produce large pressure jumps within the hot spot or the shell. For this reason, we refer to our model as the "one-shock model." If multiple shocks are launched during the acceleration phase and do not merge into one before reaching the shell center but instead converge to the center at different times, the one-shock model may not be valid. After interacting with the shell, the return shock travels within the shell material and eventually reaches the shell's outer surface.

Two shell configurations have been considered: the thin incompressible shell and the thick compressible shell. The thin shell model assumes that the shock reaches the outer shell surface immediately and that the whole shell acts like a rigid piston on the hot spot. This model is simple and provides useful physical insight into the ignition problem. However, it leads to a significant underestimation of the ignition energy requirements for two reasons: First, this model assumes that the entire shell kinetic energy is transformed into hot-spot internal energy at stagnation. Second, it does not include the shell decompression after the return shock has passed through the shell. ICF capsules are usually better described by the thick compressible shell model where the shock propagating through the shell divides it into two regions that provide compression work at different rates. At stagnation, the shock is still within the shell, and only the shocked part has released all its kinetic energy to the hot spot.

In Sec. 1, we determine the shell dynamics using the simple thin incompressible shell model. In Sec. 2, we derive the thick compressible shell model and determine all the relevant capsule properties, once the conditions at the beginning of the deceleration phase are known.

1. The Thin Incompressible Shell Model

To gain some physical insight into the shell dynamics, we consider the simple model of an incompressible shell of finite mass but infinitesimally small thickness.

The motion of the thin incompressible shell is governed by Newton's law balancing the shell inertia with the hot-spot pressure force:

$$M_{sh}\ddot{R}_{hs} = 4\pi R_{hs}^2 P_{hs},\qquad(15)$$

where M_{sh} is the shell mass. Here M_{sh} is constant and, according to the thin-shell approximation, the shell's center of mass coincides with the hot-spot radius. Note that the pressure applied to the shell's outer surface has been neglected since the laser is turned off during the deceleration phase. Equation (15) is combined with the hot-spot energy balance [Eq. (14)], which we rewrite in the following compact form:

$$\frac{d}{dt}\left[P_{hs}R_{hs}^5\right] = \Sigma_\alpha\, P_{hs}^2 R_{hs}^5.\qquad(16)$$

Equations (15) and (16) constitute a closed system of coupled differential equations that can be easily solved to determine the hot-spot pressure and shell position.

2. The Thick Compressible Shell Model

The thin incompressible shell model provides a useful qualitative understanding of the deceleration phase and hot-spot ignition. If the shell is incompressible, however, its mass supplies a uniform PdV work rate to the hot spot, and the thin shell model leads to optimistic predictions about the onset of ignition. For a more accurate quantitative estimate of the ignition conditions, it is appropriate to use a compressible model, including the return shock propagation through the shell. After the interaction with the shell's inner surface, the return shock travels within the shell material and eventually reaches the shell's outer surface. We let $R_k(t)$ denote the shock position within the shell. The shell material with $r < R_k$ is shocked and compressed, while the material with $r > R_k$ is in a "free-fall" condition. A free-fall condition is the state of the shell in the absence of a hot spot. Since the shock wave reflected from the center carries the information regarding the high pressure within the hot spot, it is reasonable to assume that the unshocked material is not aware of the presence of the hot spot and moves at constant velocity toward the center.

The shocked part of the shell behaves as a thin shell and acts like a piston on the hot spot. The unshocked part is in the free-fall (ff) condition and provides compression work rate through the flow of momentum across the shock. This flow of momentum, however, is proportional to $[\rho_{ff}]_{R_k}$ and for a given

implosion velocity can be small if the unshocked shell density ρ_{ff} is small. In simple words, a thick compressible shell does not act as a uniform piston. The material near the hot-spot surface provides PdV work at a faster rate than the material on the opposite side of the shock. The PdV work would be grossly overestimated if we were to assume that the entire shell mass is uniformly compressing the hot spot, as in the thin incompressible shell model.

a. Free-fall conditions. Free-fall conditions describe the dynamics of the unshocked part of the shell. Here a distinction is made between the coasting phase and free-fall conditions. The coasting phase represents the time interval after the laser is turned off and before the return shock has interacted with the shell. The free-fall conditions apply to the unshocked part of the shell after the shock–shell interaction. In the absence of the return shock, the shell travels inward at approximately constant velocity while its thickness increases due to the expansion of the shell material into its surroundings. We consider the following simple form for the density profile of a free-falling shell:

$$\rho_{ff}(r,t) = \frac{3M_{sh}}{\pi r^2}\frac{\left[r-R_{in}(t)\right]^2\left[R_{out}(t)-r\right]}{\Delta_{ff}^4},\qquad(17)$$

where M_{sh} is the shell mass, $\Delta_{ff} = R_{out}(t) - R_{in}(t)$ is the free-fall shell thickness, and R_{out}, R_{in} are the trajectories of the outer and inner free-falling surfaces. The density profile described by Eq. (17) accurately reproduces the results of numerical simulations obtained using the code *LILAC*.

During the coasting and deceleration phase, the absence of an applied pressure causes the shell surfaces to expand at the speed of sound, suggesting that the shell thickness increases at the rate

$$\frac{d\Delta_{ff}}{dt} = \mu\left\langle C_{s(ff)}\right\rangle,\qquad(18)$$

where $\left\langle C_{s(ff)}\right\rangle$ is the average unshocked-shell sound speed and μ is a proportionality constant. Typically the free-fall sound speed is much smaller than the shock velocity through the shell so there is no significant thickening of the shell during the deceleration phase as compared to the coasting phase. Furthermore, the shell sound speed during the free-fall phase is much lower than the implosion velocity. Therefore, changes in the

shell's internal energy do not significantly affect the free-falling shell's kinetic energy. It follows that the change in shell thickness, while significant during the coasting phase, can be neglected during the deceleration phase, and $\Delta_{\mathrm{ff}} \simeq \Delta_0 = constant$ from the shock–shell interaction time to the stagnation time. The inner and outer free-fall surface trajectories can therefore be approximated with linear functions of time:

$$R_{\mathrm{in}} \simeq R_0 - V_{\mathrm{imp}}t, \quad R_{\mathrm{out}} \simeq R_0 + \Delta_0 - V_{\mathrm{imp}}t, \quad (19)$$

where R_0 is the position of the inner shell surface at the beginning of the deceleration phase.

Since the free-fall profiles describe the conditions of the unshocked shell material, it is reasonable to assume that the free-fall conditions are isentropic. If, for simplicity, we use an ideal gas equation of state for the shell, the shell pressure evolves according to the simple adiabatic equation

$$P_{\mathrm{ff}}(r,t) = \beta_{\mathrm{ff}} \rho_{\mathrm{ff}}(r,t)^{5/3}, \quad (20)$$

where P_{ff} and β_{ff} are the free-fall pressure and adiabat, respectively. Here, for simplicity, we assume that the free-fall adiabat is uniform and equal to its value (in flight) at the beginning of the deceleration phase $\beta_{\mathrm{ff}} = \beta_{\mathrm{if}}$.

b. Shocked-shell equations of motion. The shock front divides the shell into two parts, which have different dynamics. The shocked shell material encloses the hot spot and produces the true piston action of the shell. The shocked material is usually much denser than the unshocked material. The latter is described by the free-fall conditions mentioned earlier and contributes to the hot-spot compression work through the flow of momentum across the shock front. The contribution of the free-fall shell to the hot-spot compression is dominant during the initial stage of the deceleration phase, when the mass of the shocked shell is small. At later times, however, it is the shocked shell that provides most of the compression work.

As shown in Ref. 8, ablation off the shell's inner surface into the hot spot determines the hot-spot mass. This is typically a small fraction of the shell mass until a burn wave begins to propagate through the shell and the hot spot is filled with ablated material. This raises its density to a level comparable with the shell density. Thus, mass ablation off the shell into the hot spot significantly affects the shell dynamics only after the onset of the ignition process and during burn-wave propaga-

tion in the shell, stages that are not considered in this article. Here, we neglect the effect of mass ablation on the shell's dynamics and approximate the fluid velocity at the shell's inner surface (equal to the hot-spot radius) with the surface velocity:

$$U_{\mathrm{ss}}(R_{\mathrm{hs}},t) = \dot{R}_{\mathrm{hs}} - V_a \simeq \dot{R}_{\mathrm{hs}}, \quad (21)$$

where the subscript "ss" stands for *shocked shell* and "hs" for *hot spot*. Since the shocked material is dense, it is appropriate to approximate the shocked part of the shell as a thin shell. In the thin-shell approximation, the shocked shell's thickness is assumed to be much smaller than its radius. Here, the shocked shell extends from the hot-spot radius R_{hs} to the shock front R_k, and the fluid velocity within the shocked shell can be approximated by its Taylor expansion:

$$U_{\mathrm{ss}}(r,t) \simeq \dot{R}_{\mathrm{hs}} + \left[\frac{\partial U}{\partial r}\right]_{R_{\mathrm{hs}}} (r - R_{\mathrm{hs}}). \quad (22)$$

Since the flow is isentropic within the shocked shell, it is straightforward to determine the spatial derivatives from the entropy conservation equation

$$\left[\partial_t \left(P^{3/5}r^2\right) + \partial_r \left(P^{3/5}r^2 U\right) = 0\right],$$

leading to

$$\left[\frac{\partial U}{\partial r}\right]_{R_{\mathrm{hs}}} = -\frac{1}{P_{\mathrm{hs}}(t)^{3/5} R_{\mathrm{hs}}(t)^2} \frac{d}{dt}\left\{P_{\mathrm{hs}}(t)^{3/5} R_{\mathrm{hs}}(t)^2\right\}. \quad (23)$$

Using the hot-spot-energy equation [Eq. (14)] to eliminate $\dot{P}_{\mathrm{hs}}$ in Eq. (23) and substituting (23) into (22) leads to the following simple form of the post-shock velocity:

$$U_{\mathrm{ss}}(R_k,t) = \dot{R}_{\mathrm{hs}} \frac{R_k}{R_{\mathrm{hs}}} - \frac{3}{5}\Sigma_\alpha P_{\mathrm{hs}}(R_k - R_{\mathrm{hs}}). \quad (24)$$

Because of the mass flow through the shock front, the mass of the shocked part M_{ss} increases with time. The variation of the shocked shell's mass is determined by the mass flow through the shock front:

$$\dot{M}_{\mathrm{ss}} = 4\pi R_k^2 \rho_{\mathrm{ff}}(R_k,t)\left[\dot{R}_k + V_{\mathrm{imp}}\right], \quad (25)$$

where $\rho_{ff}(R_k,t)$ is the unshocked density given by Eq. (17) calculated at the shock front. Here, the subscript "ff" (free fall) refers to the unshocked material.

The momentum balance of the shocked shell is obtained by integrating the momentum conservation equation from the hot-spot radius to the shock front, yielding

$$\frac{d}{dt}\left[M_{ss}\langle U_{ss}\rangle\right] + \dot{M}_{ss}V_{imp} = 4\pi R_{hs}^2 P_{hs}, \qquad (26)$$

where $\langle U_{ss}\rangle \simeq 0.5\left[U_{ss}(R_{hs},t) + U_{ss}(R_k,t)\right]$ is an average velocity of the shocked shell. In the derivation of Eq. (26), the shell's free-fall pressure has been neglected with respect to the hot-spot pressure, and the velocity is assumed uniform and equal to the implosion velocity throughout the free-fall part of the shell. The average shocked-shell velocity can be rewritten using Eqs. (21) and (24), yielding

$$\langle U_{ss}\rangle = \dot{R}_{hs}\frac{R_{hs}+R_k}{2R_{hs}} - \frac{3}{5}\Sigma_\alpha P_{hs}\frac{R_k-R_{hs}}{2}. \qquad (27)$$

The next step is to determine the shock position $R_k(t)$ using the Rankine–Hugoniot relations at the shock front. We assume that the return shock is strong and write the shock velocity as

$$\dot{R}_k \simeq -V_{imp} + \sqrt{\frac{4P_{ss}(R_k,t)}{3\rho_{ff}(R_k,t)}}. \qquad (28)$$

The quantity $P_{ss}(R_k,t)$ represents the pressure in the shocked shell calculated at the shock front. This pressure can be determined using another Hugoniot relation relating the velocities before $(-V_{imp})$ and after $[U_{ss}(R_k,t)]$ the shock:

$$U_{ss}(R_k,t) \simeq -V_{imp} + \sqrt{\frac{3P_{ss}(R_k,t)}{4\rho_{ff}(R_k,t)}}. \qquad (29)$$

Thus, the post-shock pressure $P_{ss}(R_k,t)$ can be determined from Eq. (29) and substituted into Eq. (28), leading to the following equation for the shock position:

$$\dot{R}_k = \frac{V_{imp}}{3} + \frac{4}{3}U_{ss}(R_k,t), \qquad (30)$$

where the post-shock velocity $U_{ss}(R_k,t)$ is given in Eq. (24). The last equation needed to close the system comes from the hot-spot energy balance [Eq. (14)] (derived earlier) relating the hot-spot pressure $P_{hs}(t)$ to the hot-spot radius $R_{hs}(t)$. Equations (14), (17), (24)–(27), and (30) represent a complete set of equations that describe the evolution of all the relevant hydrodynamic quantities during the deceleration phase and the onset of ignition. For convenience, the complete model is summarized in the following subsection.

c. Summary of the thick shell model. We summarize below all the relevant equations of the thick shell model, consisting of a set of four ordinary differential equations governing the evolution of the following hydrodynamic quantities:

1. The hot-spot pressure $P_{hs}(t)$, which obeys the following ordinary differential equation (ODE):

$$\dot{P}_{hs} + 5P_{hs}\frac{\dot{R}_{hs}}{R_{hs}} = \Sigma_\alpha P_{hs}^2. \qquad (31)$$

2. The hot-spot radius $R_{hs}(t)$ equal to the shocked-shell inner-surface radius governed by Newton's law:

$$M_{ss}\frac{d}{d\tau}\langle U_{ss}\rangle + \dot{M}_{ss}\left[\langle U_{ss}\rangle + V_{imp}\right] = 4\pi P_{hs}R_{hs}^2, \qquad (32)$$

where $\langle U_{ss}\rangle$ is the average shocked-shell velocity,

$$\langle U_{ss}\rangle = \dot{R}_{hs}\frac{R_{hs}+R_k}{2R_{hs}} - \frac{3}{10}\Sigma_\alpha P_{hs}(R_k-R_{hs}), \qquad (33)$$

and R_k is the shock position.

3. The shocked-shell mass $M_{ss}(t)$, which obeys mass conservation:

$$\dot{M}_{ss} = 4\pi R_k^2 \rho_{ff}(R_k,t)\left[\dot{R}_k + V_{imp}\right]. \qquad (34)$$

4. The shock position within the shell $R_k(t)$ derived from Hugoniot relations:

$$\dot{R}_k = \frac{V_{imp}}{3} + \frac{4}{3}U_{ss}(R_k,t), \qquad (35)$$

where $U_{ss}(R_k,t)$ is the post-shock velocity,

$$U_{ss}(R_k,t) = \dot{R}_{hs}\frac{R_k}{R_{hs}} - \frac{3}{5}\Sigma_\alpha P_{hs}(R_k - R_{hs}).\quad(36)$$

The unshocked shell material is described by the *free-fall* conditions:

$$\rho_{ff}(r,t) = \frac{3M_{sh}}{\pi r^2}\frac{[r - R_{in}(t)]^2[R_{out}(t)-r]}{\Delta_0^4},\quad(37)$$

where M_{sh} is the total shell mass, $\Delta_0 = R_{out}(t)-R_{in}(t)$ is the free-fall shell thickness (approximately constant), and $R_{in}(t) = R_0-V_{imp}t$ is the inner-surface trajectory starting from the initial radius R_0 at the beginning of the deceleration phase.

A set of initial conditions at the beginning of the deceleration phase corresponding to the shell–shock interaction time must be provided to solve the system of equations:

1. the inner-surface, free-fall (or implosion) velocity $-V_{imp}$,
2. the inner shell radius R_0,
3. the shell thickness Δ_0,
4. the shell mass M_{sh}, and
5. the hot-spot pressure P_0.

The solution of the four differential equations yields the time evolution of the shock position, hot-spot radius, and pressure. The last two quantities can be used to determine the evolution of all other relevant hydrodynamic quantities inside the hot spot, such as temperature, density, ablation velocity, density-gradient scale length, and areal density as described in Ref. 8.

Ignition Scaling Using the Thin Incompressible Shell Model

In this section, we first determine the ignition criterion in terms of the initial conditions at the beginning of the deceleration phase for the thin incompressible shell model. The ignition criterion has a very simple form and simple physical interpretation. Next, we derive a scaling law in terms of the shell's kinetic energy and an entropy function. The latter does not represent the shell adiabat since the shell is assumed incompressible. It will be shown in the section entitled **Ignition Scaling Using the Compressible Shell Model**, however, that this entropy function is directly proportional to the shell

adiabat at stagnation when the finite compressibility of the shell is included.

1. Ignition Criterion

The thin shell model can be simplified by eliminating P_{hs} between Eqs. (15) and (16) and by using the following dimensionless variables:

$$\hat{R}_{hs} \equiv R_{hs}/R_0, \quad \tau = V_{imp}t/R_0.\quad(38)$$

A straightforward manipulation of Eqs. (15) and (16) leads to the following single ordinary differential equation for the hot-spot radius:

$$\frac{d}{d\tau}\left(\hat{R}_{hs}^3\frac{d^2\hat{R}_{hs}}{d\tau^2}\right) = \frac{Y_\alpha}{\hat{\varepsilon}_0}\hat{R}_{hs}\left(\frac{d^2\hat{R}_{hs}}{d\tau^2}\right)^2,\quad(39)$$

where

$$Y_\alpha \equiv \frac{\Sigma_\alpha P_0 R_0}{V_{imp}}\hat{\varepsilon}_0^2 = \frac{\tau_i^0}{\tau_\alpha^0}\hat{\varepsilon}_0^{3/2}, \quad \hat{\varepsilon}_0 = \frac{M_{sh}V_{imp}^2}{4\pi P_0 R_0^3},\quad(40)$$

$$\tau_i^0 = \left[\frac{M_{sh}}{4\pi P_0 R_0}\right]^{1/2}, \quad \tau_\alpha^0 = \frac{1}{\Sigma_\alpha P_0}.\quad(41)$$

Here $\hat{\varepsilon}_0$ represents the ratio between the initial shell kinetic energy and the initial hot-spot internal energy, which is much greater than unity in typical ICF implosions. (Small values of $\hat{\varepsilon}_0$ require that the hot-spot radius at the beginning of the free-fall phase be very close to the stagnation hot-spot radius. This does not occur in typical ICF implosions.) The times τ_i^0 and τ_α^0 represent the inertial time of the shell and the alpha-particle heating time at the beginning of the deceleration phase. The shell trajectory is determined by solving Eq. (39) with the following initial conditions:

$$\hat{R}_{hs}(0) = 1, \quad \dot{\hat{R}}_{hs}(0) = -1, \quad \ddot{\hat{R}}_{hs}(0) = 1/\hat{\varepsilon}_0,\quad(42)$$

where the "dot" indicates a derivative with respect to τ.

It is important to notice that as long as the alpha heating is smaller than the compression work, the right-hand side of Eq. (39) can be neglected and the shell trajectory is given by

$$\hat{R} = \sqrt{1 - 2\tau + \tau^2\left(1 + \hat{\varepsilon}_0^{-1}\right)}, \tag{43}$$

leading to the following values of the stagnation time, radius, acceleration, and pressure:

$$t_{\mathrm{stag}} = \frac{R_0}{V_{\mathrm{imp}}}\frac{\hat{\varepsilon}_0}{1+\hat{\varepsilon}_0}, \qquad R_{\mathrm{stag}} = \frac{R_0}{\sqrt{1+\hat{\varepsilon}_0}}, \tag{44a}$$

$$g_{\mathrm{stag}} = \left(1+\hat{\varepsilon}_0\right)^{3/2}\frac{R_0}{\left(\tau_i^0\right)^2}, \qquad P_{\mathrm{stag}} = P_0\left(1+\hat{\varepsilon}_0\right)^{5/2}. \tag{44b}$$

Equations (44) yield scaling relations for the stagnation values of the hydrodynamic quantities in terms of the shell and hot-spot properties at the beginning of the deceleration phase. Such relations are valid as long as the hot spot is not ignited. If the alpha heating becomes important, the right-hand side of Eq. (39) must be retained and the stagnation pressure and deceleration are significantly larger.

It is easy to show that, for a given $\hat{\varepsilon}_0$, the solution of Eq. (39) develops an explosive instability when the parameter Υ_α exceeds a critical value. Both parameters $\hat{\varepsilon}_0$ and Υ_α are functions of the shell and hot-spot properties at the beginning of the deceleration phase (M_{sh}, V_{imp}, R_0, and P_0). A typical singular explosive solution (dashed line in Fig. 87.47) shows the shell ejected outward at an infinite velocity. Such solutions correspond to the thermal instability of the hot spot, which we denote as "ignition." The singularity is due to the fact that the fusion reaction rate $\langle\sigma v\rangle$ is taken to be proportional to T^2, and, therefore, it diverges to infinity with temperature. In reality, $\langle\sigma v\rangle$ is bounded at high temperatures and the shell ejection velocity is finite. Nevertheless, the occurrence of the singularity in the solution of Eq. (39) represents a simple and robust definition of ignition for the thin shell model. We therefore conclude that the hot spot is ignited when the solution of Eq. (39) is singular. The numerical solution of Eq. (39) indicates that singular solutions develop when the following approximate condition is satisfied:

$$\Upsilon_\alpha\left[1+\left(\frac{3}{5}\right)^{1/3}\hat{\varepsilon}_0^{-1}\right]^{3/2} > \sqrt{3}, \tag{45a}$$

which reduces to

$$\Upsilon_\alpha > \sqrt{3} \tag{45b}$$

in the limit $\hat{\varepsilon}_0 \gg 1$. Equations (45) represent the ignition conditions in terms of the shell and hot-spot properties at the beginning of the deceleration phase. The physical interpretation of the ignition threshold is straightforward. We rewrite the hot-spot-energy equation [Eq. (14)] in the following intuitive form:

$$\frac{1}{E_{\mathrm{hs}}}\frac{dE_{\mathrm{hs}}}{dt} = \Sigma_\alpha P_{\mathrm{hs}} - 2\frac{\dot{R}_{\mathrm{hs}}}{R_{\mathrm{hs}}}, \tag{46}$$

where $E_{\mathrm{hs}} = (4\pi/3)P_{\mathrm{hs}}R_{\mathrm{hs}}^3$ is the hot-spot energy. After stagnation, the second term on the right-hand side is negative ($\dot{R}_{\mathrm{hs}} > 0$ after stagnation) and represents the inverse hot-spot decompression time $\left(\tau_{\mathrm{decomp}} = R_{\mathrm{hs}}/2\dot{R}_{\mathrm{hs}}\right)$ due to the outward motion of the shell pushed by the hot-spot pressure. This decompression time can be estimated by setting

$$\tau_{\mathrm{decomp}} \sim 0.5\sqrt{R_{\mathrm{hs}}/\ddot{R}_{\mathrm{hs}}}$$

and using Eq. (15), leading to

$$\tau_{\mathrm{decomp}} = \frac{1}{2}\sqrt{\frac{M_{\mathrm{sh}}}{4\pi P_{\mathrm{hs}}R_{\mathrm{hs}}}}. \tag{47}$$
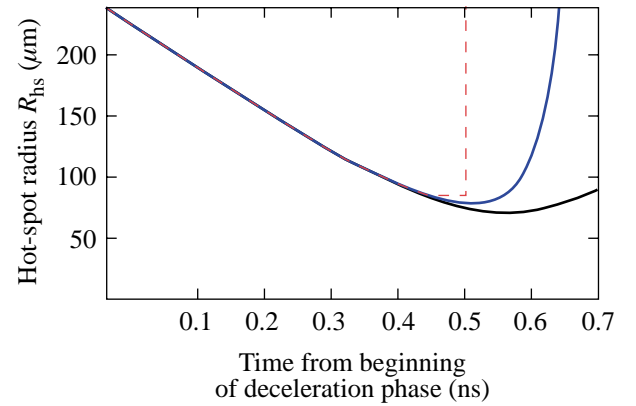

TC5708

Figure 87.47
Thin incompressible shell model prediction for the evolution of the hot-spot radius for NIF-like capsules [obtained by solving Eq. (39)]. The dashed line represents an ignited solution with a singularity after stagnation. The solid lines represent two non-ignited solutions.

Note that the first term on the right-hand side of Eq. (46) represents the inverse alpha-particle heating time

$$\tau_\alpha = 1/\Sigma_\alpha P_{\text{hs}}.$$

Ignition occurs right after stagnation if the alpha heating time is shorter than the decompression time:

$$\tau_\alpha(\text{stag}) < \tau_{\text{decomp}}(\text{stag}). \qquad (48)$$

If Eq. (48) is satisfied, a thermal instability (the ignition process) is triggered because the hot-spot pressure starts to increase and leads to a shorter alpha heating time $\tau_\alpha \sim 1/P_{\text{hs}}$. The decompression time is proportional to $1/\sqrt{P_{\text{hs}}}$ and decreases less than the alpha heating time. This leads to a further increase in pressure and a thermal explosive instability. To estimate the ignition threshold, we use the stagnation values (without alpha particles) given in Eqs. (44) to find τ_α (stag):

$$\tau_\alpha(\text{stag}) \approx \frac{1}{\Sigma_\alpha P_0 \left(1+\hat{\varepsilon}_0\right)^{5/2}} = \frac{\tau_\alpha^0}{\left(1+\hat{\varepsilon}_0\right)^{5/2}}. \qquad (49)$$

Similarly, we find $\tau_{\text{decomp}}(\text{stag})$:

$$\tau_{\text{decomp}}(\text{stag}) \approx \frac{1}{2}\left(\frac{R_{\text{stag}}}{g_{\text{stag}}}\right)^{1/2} = \frac{\tau_i^0}{2\left(1+\hat{\varepsilon}_0\right)}, \qquad (50)$$

where τ_i^0 [defined in Eq. (41)] represents the decompression time if the shell stagnates at time $t = 0 \left[\tau_{\text{decomp}}(0) = \tau_i^0\right]$. Substituting Eqs. (49) and (50) into (48) yields the approximate ignition condition

$$\frac{\tau_{\text{decomp}}(0)}{\tau_\alpha(0)}\left(1+\hat{\varepsilon}_0\right)^{3/2} = \Upsilon_\alpha\left(1+\hat{\varepsilon}_0^{-1}\right)^{3/2} > 2, \qquad (51)$$

where the identity $\tau_\alpha^0 \equiv \tau_\alpha(0)$ has been used and the term $\left(1+\hat{\varepsilon}_0\right)^{3/2}$ represents the amplification factor of the ratio τ_i/τ_α due to the hot-spot compression by the shell. Observe that condition (51) is similar to the numerical fit given in (45a) and yields approximately the same ignition threshold ($\Upsilon_\alpha > 2$) in the limit of $\hat{\varepsilon}_0 \gg 1$.

2. Ignition Scaling

We consider the marginal ignition criterion given in Eq. (45b) in the relevant ICF limit $\hat{\varepsilon}_0 \gg 1$ and rewrite Υ_α [defined in Eq. (40)] in the following form:

$$\Upsilon_\alpha = \frac{\Sigma_\alpha}{(2\pi)^2} \frac{E_k^2}{P_0 R_0^5 V_{\text{imp}}}, \qquad (52)$$

where $E_k = M_{\text{sh}} V_{\text{imp}}^2 / 2$ is the shell's kinetic energy. Using the thin-shell approximation, the shell mass can be written as

$$M_{\text{sh}} \simeq 4\pi\rho_{\text{sh}}(0) R_0^3 / A_0, \qquad (53)$$

where $\rho_{\text{sh}}(0)$ and $A_0 = R_0/\Delta_0$ are the shell density and aspect ratio at the beginning of the deceleration phase (here Δ_0 is the shell thickness). Equation (53) can also be cast in terms of shell kinetic energy by multiplying both sides by V_{imp}^2 and then using it to derive the initial hot-spot radius R_0:

$$R_0 \simeq \left(\frac{A_0 E_k}{2\pi\rho_{\text{sh}}(0) V_{\text{imp}}^2}\right)^{1/3}. \qquad (54)$$

Substituting Eq. (54) into Eq. (52) and rewriting the ignition condition $\Upsilon_\alpha = constant$ in terms of the kinetic energy yields

$$E_k \simeq \frac{2\pi\Upsilon_\alpha^3}{\Sigma_\alpha^3} \frac{\beta_0^3}{V_{\text{imp}}^7}, \qquad (55)$$

where $\Upsilon_\alpha \simeq \sqrt{3}$ for ignition and

$$\beta_0 \equiv \frac{P_0}{\left[\rho_{\text{sh}}(0)/A_0\right]^{5/3}} \qquad (56)$$

has the dimensions of an adiabat. Note that the pressure P_0 is the hot-spot pressure at time $t = 0$ and not the shell pressure. Thus, at this stage, the parameter β_0 cannot be related to the shell adiabat as should be expected when approximating the shell with an incompressible layer. The scaling (56), though dimensionally similar to the HTL stagnation scaling [Eq. (5)], is still inconclusive and deserves further analysis as shown in the next section, where the effects of finite shell compressibility are retained.

Ignition Scaling Using the Compressible Shell Model

Since the right-hand side of Eq. (55) represents the minimum kinetic energy required for ignition, it is appropriate to determine A_0 in order to minimize the ignition requirements. The optimum A_0 can be determined by making use of the thick shell model described earlier [Eqs. (31)–(37)] and the following simple argument.

If the shell is too thin, the return shock reaches the outer shell surface before stagnation, causing the shell to rapidly expand outward, decompressing the hot spot and stopping the ignition process. If the shell is too thick, stagnation (and therefore ignition) is reached when the shock is still within the shell and the unshocked part of the shell is still free falling. In this scenario, ignition is triggered with a surplus of kinetic energy in the free-fall part of the shell. Ignition using the minimum kinetic energy occurs when the return shock is exactly at the shell's outer surface at the same time the shell reaches the stagnation point. We conclude that the optimum shell thickness is such that the shock reaches the outer shell surface at stagnation.

Because the shock position is the new information needed to optimize A_0 and minimize the shell's kinetic energy, the ignition condition needs to be determined using the compressible thick shell model. The next step is to rewrite the thick shell model in dimensionless form using the following definitions:

$$\hat{R}_{hs} = R_{hs}/R_0, \quad \hat{R}_k = R_k/R_0, \quad \hat{P}_{hs} = P_{hs}/P_0, \quad (57a)$$

$$\tau = V_{imp}t/R_0, \quad \hat{M} = M_{ss}/M_{sh}, \quad (57b)$$

where R_0 and P_0 are the shell's inner surface and hot-spot pressure at the beginning of the deceleration phase. A simple manipulation of Eqs. (31)–(37) using the definitions in (57) yields a closed set of four differential equations,

$$\frac{d}{d\tau}\left\{\hat{M}\left[\dot{\hat{R}}_{hs}\frac{\hat{R}_{hs}+\hat{R}_k}{2\hat{R}_{hs}}-\frac{3}{10}\frac{\Upsilon_\alpha}{\hat{\varepsilon}_0^2}\hat{P}_{hs}\left(\hat{R}_k-\hat{R}_{hs}\right)+1\right]\right\}$$

$$=\frac{\hat{P}_{hs}\hat{R}_{hs}^2}{\hat{\varepsilon}_0}, \quad (58)$$

$$\dot{\hat{R}}_k = \frac{1}{3}+\frac{4}{3}\dot{\hat{R}}_{hs}\frac{\hat{R}_k}{\hat{R}_{hs}}-\frac{4}{5}\frac{\Upsilon_\alpha}{\hat{\varepsilon}_0^2}\hat{P}_{hs}\left(\hat{R}_k-\hat{R}_{hs}\right), \quad (59)$$

$$\dot{\hat{M}} = 12A_0^4\left(\hat{R}_k+\tau-1\right)^2\left|1+A_0^{-1}-\tau-\hat{R}_k\right|$$

$$\times\left(\dot{\hat{R}}_k+1\right)H\left(1-\hat{M}\right), \quad (60)$$

$$\dot{\hat{P}}_{hs}+5\hat{P}_{hs}\frac{\dot{\hat{R}}_{hs}}{\hat{R}_{hs}}=\frac{\Upsilon_\alpha}{\hat{\varepsilon}_0^2}\hat{P}_{hs}^2, \quad (61)$$

representing the evolution of the shocked shell's inner radius $\hat{R}_{hs}$, shock position $\hat{R}_k$, shocked shell mass $\hat{M}$, and hot-spot pressure $\hat{P}_{hs}$. The step function $H\left(1-\hat{M}\right)$ in Eq. (60) limits the magnitude of the shocked shell mass to the total shell mass. That is, when $M_{ss}=M_{sh}$ (i.e., $\hat{M}=1$), the right-hand side of Eq. (60) vanishes and the shocked shell mass remains constant and equal to the total shell mass. Equations (58)–(61) can be solved using the following set of initial conditions:

$$\hat{R}_{hs}(0)=1, \quad \dot{\hat{R}}_{hs}(0)=0, \quad \hat{R}_k(0)=1,$$

$$\hat{M}(0)=0, \quad \hat{P}_{hs}(0)=1. \quad (62)$$

The initial condition $\dot{\hat{R}}_{hs}=0$ needs a clarification. Before the interaction with the return shock, the shell density vanishes on the inner surface. As a result of the interaction with the shock, the shell's inner surface is stopped, so the condition $\dot{\hat{R}}_{hs}=0$ is applicable right after the interaction with the shock. After this brief stop, the inner shell surface is set in motion by the imploding high-density shell material that is not stopped by the return shock.

Observe that Eqs. (58)–(61) depend on three dimensionless parameters Υ_α, $\hat{\varepsilon}_0$, and A_0, which need to be determined to satisfy the following two conditions: (1) the hot spot must be ignited, and (2) the return shock must be on the outer surface at stagnation to assure that the kinetic energy is minimized. The first condition requires that the solution of Eqs. (58)–(61) be singular and the shell be ejected outward at infinite velocity after stagnation. The second requires that $\hat{M}=1$ at stagnation, implying that the entire shell has been shocked.

We solve Eqs. (58)–(61) with the software program MATHEMATICA in the limit of $\hat{\varepsilon}_0 \gg 1$, which is the correct limit for ICF implosions since the shell's kinetic energy is much larger than the hot-spot internal energy at the beginning of the deceleration phase. We find that the singular solutions with $\hat{M} = 1$ at stagnation occur when

$$A_0 \approx 0.39\sqrt{\hat{\varepsilon}_0}\,, \quad Y_\alpha \approx 2.60\,. \tag{63}$$

Other results from the solution of Eqs. (58)–(61) are shown in Figs. 87.48–87.50. Figures 87.48 and 87.49 plot the evolution of the shocked shell mass and hot-spot pressure. Figure 87.50 shows the trajectories of the hot-spot radius and the shock front near stagnation. Analysis of the solution to the thick shell equations suggests that the stagnation scaling of the hot-spot pressure, hot-spot radius, and shock position are given by the following:

$$P_{hs}(\text{stag}) \approx 1.02\, P_0 \hat{\varepsilon}_0^{5/2}\,, \tag{64a}$$

$$R_{hs}(\text{stag}) \approx 1.23\, R_0/\sqrt{\hat{\varepsilon}_0}\,, \tag{64b}$$

$$R_k(\text{stag}) \approx 1.40\, R_0/\sqrt{\hat{\varepsilon}_0}\,. \tag{64c}$$

Observe that the relations for the stagnation values of P_{hs} and R_{hs} are similar (except for a numerical factor) to the ones obtained earlier [Eqs. (44)] with the thin shell model and

$\hat{\varepsilon}_0 \gg 1$. The ignition condition for Y_α in Eq. (63) is also similar to (but with a different numerical value) that derived with the thin shell model and leads to the same scaling for the minimum energy required for ignition:

$$E_k \approx \frac{2\pi Y_\alpha^3}{\Sigma_\alpha^3} \frac{\beta_0^3}{V_{imp}^7}\,, \tag{65}$$

where β_0 is defined in Eq. (56). The new result here is that the shell's aspect ratio A_0 at the beginning of the deceleration phase is related to the other shell properties through the first condition in Eq. (63). Furthermore, the position of the outer

TC5703

Figure 87.49
Thick compressible shell model results. Evolution of the hot-spot pressure, obtained from Eqs. (58)–(61). The vertical dashed line represents the shock breakout time (also stagnation time).
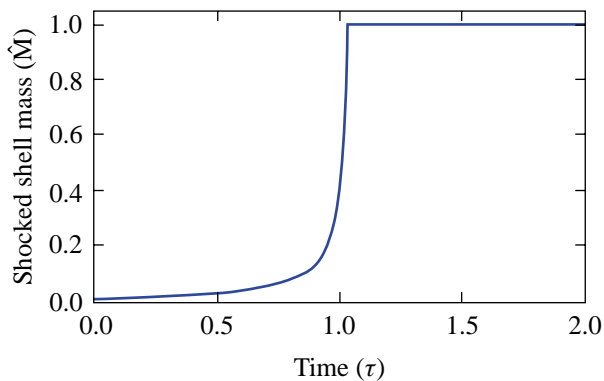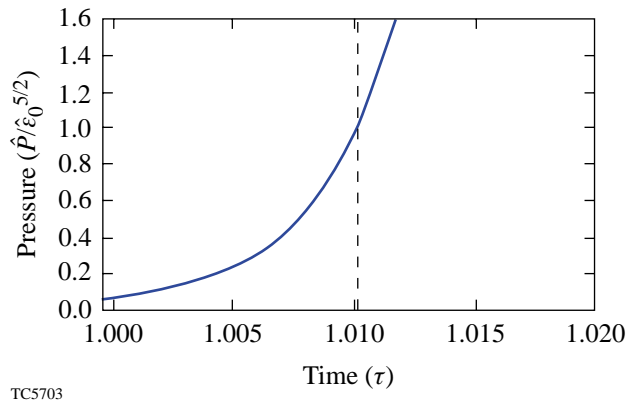

TC5702

Figure 87.48
Thick compressible shell model results. Plot of the shocked shell mass versus time. Time $t = 0$ corresponds with the beginning of the deceleration phase. When $\hat{M} = 1$, the entire shell has been shocked.
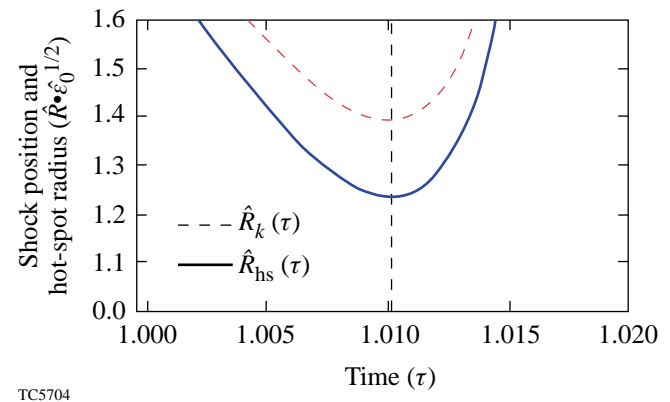

TC5704

Figure 87.50
Thick compressible shell model results. Trajectories of the shock and the hot-spot radius, obtained from Eqs. (58)–(61). The vertical dashed line represents the shock breakout time (also stagnation time).

shell surface coincides with the shock position R_k and is determined in Eq. (64c). This latest result is essential to determine the ignition scaling in terms of the stagnation properties.

Setting the shell mass at the beginning of the deceleration phase equal to the stagnation mass,

$$4\pi \frac{R_0^3}{A_0}\rho_{\rm sh}(0) \approx \frac{4\pi}{3}\left[R_k({\rm stag})^3 - R_{\rm hs}({\rm stag})^3\right]\rho_{\rm sh}({\rm stag}), \quad (66)$$

and substituting Eqs. (64) into Eq. (66) leads to the following relation between the shell densities:

$$\rho_{\rm sh}(0) \approx 0.3\,\rho_{\rm sh}({\rm stag})\frac{A_0}{\hat{\varepsilon}_0^{3/2}}. \quad (67)$$

Then, using the definition of $\beta_0 \equiv A_0^{5/3}P_0/\rho_{\rm sh}(0)^{5/3}$ and Eqs. (64a) and (67), the following relation is easily derived:

$$\beta_0 \approx 7.52\,\beta_s, \quad (68)$$

where $\beta_s \equiv P_{\rm hs}({\rm stag})/\rho_{\rm sh}({\rm stag})^{5/3}$ represents the shell stagnation adiabat. Observe that the hot-spot pressure is used in the definition of the shell stagnation adiabat. While this is not an exact definition, it is sufficiently accurate because the stagnation pressure is continuous at the hot spot/shell interface.

The next step is to finalize the scaling law Eq. (65) using Eqs. (63) and (68) and the standard definition of the normalized stagnation adiabat

$$\alpha_s \equiv \frac{P({\rm Mbar})}{2.18\,\rho_{\rm sh}\left({\rm g/cm^3}\right)^{5/3}}. \quad (69)$$

A straightforward manipulation of Eq. (65) leads to the following formula for the minimum energy required for ignition:

$$E_k \approx 2.7\,({\rm kJ})\,\alpha_s^3\left[\frac{3\times10^7}{V_{\rm imp}({\rm cm/s})}\right]^7. \quad (70)$$

Equation (70) represents the marginal ignition scaling in terms of the stagnation adiabat. Observe that Eq. (70) is quite similar

in both the scaling relation as well as the numerical coefficient with the result of Ref. 5, which reads as

$$E_k \approx 2.1\,({\rm kJ})\,\alpha_s^{2.66}\left[\frac{3\times10^7}{V_{\rm imp}({\rm cm/s})}\right]^{7.2}.$$

The next step is to relate the stagnation to the in-flight adiabat and determine the "in-flight" scaling for marginal ignition.

Ignition Scaling Using the In-Flight Adiabat

Comparisons of different ignition capsules are usually based on the magnitude of the in-flight adiabat, which can be easily controlled by tuning the initial foot of the laser pulse. In this section, the stagnation adiabat is related to the in-flight adiabat, and the ignition scaling law is expressed in terms of the in-flight hydrodynamic properties of the shell.

Starting from Eq. (63) $\left(A_0 = 0.39\sqrt{\hat{\varepsilon}_0}\right)$ and the definition of $\hat{\varepsilon}_0$ [Eq. (40)], we express the hot-spot pressure at the beginning of the deceleration phase $P_{\rm hs}(0)$ in terms of the shell pressure at the same time $P_{\rm sh}(0)$:

$$P_{\rm hs}(0) \approx 0.25\,P_{\rm sh}(0)\,M_A(0)^2/A_0^3, \quad (71)$$

where $M_A(0) = V_{\rm imp}/C_s(0)$ is the shell's Mach number at the beginning of the deceleration phase and $C_s(0)$ is the shell's sound speed. Substituting Eq. (71) into Eq. (68) yields the following relation:

$$\beta_s \approx 0.034\,\beta_{\rm if}\,M_A(0)^2/A_0^{4/3}, \quad (72)$$

where $\beta_{\rm if} \equiv P_{\rm sh}(0)/\rho_{\rm sh}(0)^{5/3}$ is the shell's in-flight adiabat. It is important to emphasize that time zero represents the beginning of the deceleration phase, which starts after the coasting phase.

The next step is to relate the shell's Mach number and aspect ratio at the beginning of the deceleration phase to their values at the beginning of the coasting phase during which the laser is off and the ablation pressure vanishes. During the coasting phase, the shell travels at approximately constant velocity, while rarefaction waves propagate inside the shell from both the inner and outer surfaces since the shell pressure is much larger than the surrounding pressure. The expansion velocity induced by a rarefaction wave is

$$v_{\exp} = 3C_s\left[1-\left(\rho/\rho_{\max}\right)^{1/3}\right]$$

and depends on the location along the density profile. If we characterize the shell as the region enclosed by the two points where the density is equal to $1/e$ times the maximum density, then the expansion velocity of the inner and outer surfaces is $v_{\exp} \simeq 0.85\,C_s$. Using these definitions, the shell thickness $\Delta_{\rm sh}$ increases with time during the coasting phase, according to the following equation:

$$\frac{d\Delta_{\rm sh}}{dt} \simeq 1.7\,C_s^c, \tag{73}$$

where C_s^c is the shell sound speed during the coasting phase. Equation (73) can be further simplified by using the following dimensionless variables:

$$\hat{\Delta}_{\rm sh} = \Delta_{\rm sh}/\Delta_c, \quad \hat{R}_{\rm sh} = R_{\rm sh}/R_c,$$

where $R_{\rm sh}$ is the shell radius and R_c, Δ_c are the shell radius and thickness at the beginning of the coasting phase. Assuming that the shell adiabat is constant during the coasting phase and using the thin-shell approximation $\left[M_{\rm sh}\simeq 4\pi\rho_{\rm sh}R_{\rm sh}^2\Delta_{\rm sh}\right]$, Eq. (73) can be rewritten as

$$\frac{d\hat{\Delta}_{\rm sh}}{d\hat{R}_{\rm sh}} = -1.7\,\frac{A_c}{M_A^c}\,\frac{1}{\hat{R}_{\rm sh}^{2/3}\hat{\Delta}_{\rm sh}^{1/3}}, \tag{74}$$

where A_c and M_A^c are the shell's aspect ratio and Mach number at the beginning of the coasting phase. Equation (74) can be easily integrated to determine the evolution of the shell thickness during the coasting phase:

$$\Delta_{\rm sh} = \Delta_c\left\{1+6.8\,\frac{A_c}{M_A^c}\left[1-\left(\frac{R_{\rm sh}}{R_c}\right)^{1/3}\right]\right\}^{3/4}. \tag{75}$$

Assuming that the shell radius at the beginning of the deceleration phase is much smaller than the radius at the beginning of the coasting phase $[R_{\rm sh}(0) << R_c]$, Eq. (75) yields the asymptotic value of the shell thickness at the beginning of the deceleration phase (i.e., time $t = 0$):

$$\Delta_{\rm sh}(0) \simeq \Delta_c\left(1+6.8\,\frac{A_c}{M_A^c}\right)^{3/4}. \tag{76}$$

A relation between the aspect ratio A_c and Mach number M_A^c can be determined by matching the shell expansion rate at the beginning of the coasting phase with the one calculated at the end of the acceleration phase as explained below.

During the acceleration phase, the shell density can be obtained from the momentum conservation equation

$$\rho_{\rm sh}g = \frac{\partial P}{\partial r}, \tag{77}$$

where $P = \beta_{\rm if}\rho_{\rm sh}^{5/3}$. A simple manipulation of Eq. (77) yields the density profile

$$\rho_{\rm sh} \simeq \rho_a\left(1-\frac{R_a-r}{2\Delta_{\rm sh}}\right)^{3/2}, \tag{78}$$

where R_a is the radius of the ablation surface, ρ_a is the density at the ablation surface, and

$$\Delta_{\rm sh} \simeq \frac{3C_s^2}{4g} \tag{79}$$

is the shell thickness from the ablation surface to the $1/e$ point. The shell's aspect ratio peaks at the beginning of the main pulse when its value is proportional to the square of the Mach number. It then decays during the main pulse and the following coasting phase when the shell radius decreases and the thickness increases. The thickness can be written in terms of the shell radius by using Eq. (79) and assuming that the ablation pressure P_a increases like $1/R$ as indicated by the result of several numerical simulations. Setting $g = 4\pi R^2 P_a/M_{\rm sh}$ into Eq. (79) yields the shell thickness as a function of the radius:

$$\Delta_{\rm sh} = \frac{5}{16\pi}\,\frac{\beta_{\rm if}^{3/5}M_{\rm sh}}{\left(P_a R_{\rm sh}\right)^{3/5}}\,\frac{1}{R_{\rm sh}^{7/5}} \sim \frac{1}{R_{\rm sh}^{7/5}}. \tag{80}$$

In deriving Eq. (80), the reduction of the shell mass due to the laser ablation has been neglected. This approximation may not be appropriate for indirect-drive capsules where a large portion of the shell material is ablated off during the implosion. The rate of the shell expansion during the acceleration phase follows from Eq. (80):

$$\dot{\Delta}_{sh} \simeq -\frac{7}{5}\frac{\Delta_{sh}}{R_{sh}}\dot{R}_{sh}. \tag{81}$$

When the expansion velocity [Eq. (81)] reaches the sound speed, the shell pressure exceeds the applied ablation pressure. Typically, the laser is turned off at this point since the shell pressure is so large that the applied ablation pressure has little effect on the shell dynamics. From a mathematical standpoint, the acceleration phase turns into the coasting phase when the shell's expansion velocity calculated during acceleration phase [Eq. (81)] matches the expansion velocity calculated during the coasting phase [Eq. (73)]. The matching occurs when

$$\frac{7}{5}\frac{\Delta_{sh}}{R_{sh}} = 1.7\frac{C_s^c}{-\dot{R}_{sh}}, \tag{82}$$

which leads to the following expression for the aspect ratio at the beginning of the coasting phase:

$$A_c = 0.82\,M_A^c. \tag{83}$$

The next step is to rewrite the shell's Mach number at the beginning of the deceleration phase in terms of the hydrodynamic quantities at the beginning of the coasting phase. Using the thin-shell approximation, one finds

$$M_A(0) = M_A^c\left(\frac{R_0}{R_c}\right)^{2/3}\left(\frac{\Delta_0}{\Delta_c}\right)^{1/3}, \tag{84}$$

where $R_0 = R_{sh}(0)$ and $\Delta_0 = \Delta_{sh}(0)$. Substituting Eqs. (83), (84), and (76) into (72) leads to the following expression of the stagnation adiabat:

$$\beta_s = 0.74\,\beta_{if}\left(M_A^c\right)^{2/3}, \tag{85}$$

which can be expressed in the convenient form

$$\alpha_s = 2.8\,\alpha_{if}^{0.8}\left[\frac{V_{imp}(\text{cm/s})}{3\times10^7}\right]^{0.67}\left[\frac{100}{P(\text{Mbar})}\right]^{0.13}. \tag{86}$$

This relation is similar to the numerical fit of Herrmann et al.[5] and to the self-similar scaling found by Kemp et al.:[6]

$$\alpha_s^{HTL} = 3.2\,\alpha_{if}^{0.75}\left[\frac{V_{imp}(\text{cm/s})}{3\times10^7}\right]^{0.44}\left[\frac{100}{P(\text{Mbar})}\right]^{0.21}, \tag{87}$$

$$\alpha_s^{KMA} = 2.3\,\alpha_{if}^{0.85}\left[\frac{V_{imp}(\text{cm/s})}{3\times10^7}\right]^{0.5}\left[\frac{100}{P(\text{Mbar})}\right]^{0.1}. \tag{88}$$

The final ignition energy scaling can be found by substituting Eq. (86) into Eq. (70), yielding

$$E_k = 59\,(\text{kJ})\,\alpha_{if}^{2.4}\left[\frac{3\times10^7}{V_{imp}(\text{cm/s})}\right]^{5}\left[\frac{100}{P(\text{Mbar})}\right]^{0.39}, \tag{89}$$

which is similar to Herrmann's numerical fit

$$E_k^{HTL} = 50.8\,(\text{kJ})\,\alpha_{if}^{1.88}\left[\frac{3\times10^7}{V_{imp}(\text{cm/s})}\right]^{5.89}\left[\frac{100}{P(\text{Mbar})}\right]^{0.77}. \tag{90}$$

Observe that both Eq. (88) and (89) show a scaling relation resembling the one derived by Kemp et al. as long as the triple product $\rho_{hs}T_{hs}R_{hs}$ is a constant for marginal ignition. However, as shown in the following section, the model described in this article yields a triple product that is proportional to the implosion velocity. This is in agreement with Basko's analysis.

Assumptions About Hot-Spot Hydrodynamics

It is important to remember that Eq. (89) has been derived under three assumptions. The first relates the alpha-particle mean free path, which is assumed to be smaller than the hot-spot radius, implying that the alpha-particle energy is deposited locally. The second, that the behavior of the averaged fusion cross section is given by $\langle\sigma v\rangle \sim T^2$, is valid as long as

the volume average temperature $\bar{T}_{hs}$ is above 6 keV. The third comes from neglecting the radiation losses with respect to the alpha heating. To verify these assumptions, we use the hot-spot solution derived in Ref. 8, where all the hot-spot hydrodynamic quantities are obtained as functions of the hot-spot radius and pressure.

We start with the first of Eq. (24) of Ref. 8, calculated at the hot-spot center $\xi = 0$. Observe that Eq. (24) is an integral equation because the hot-spot mass M_{hs} is a time integral. Equation (24) can be easily converted into a simple differential equation for the central hot-spot density ρ_{hs}^0:

$$\dot{\rho}_{hs}^0 + 3\rho_{hs}^0 \frac{\dot{R}_{hs}}{R_{hs}} = 0.072\, m_i^{7/2} \kappa_0 \frac{P_{hs}^{5/2}}{\left(\rho_{hs}^0\right)^{5/2} R_{hs}^2}, \quad (91)$$

where $\kappa_0 T^{5/2}$ represents Spitzer thermal conductivity. Equation (91) can be rewritten in a convenient dimensionless form by defining the following variables:

$$\hat{\rho} = \rho_{hs}^0 / \rho_*, \quad \hat{P} = P_{hs}/P_0, \quad (92)$$

$$\tau = t V_{imp}/R_0, \quad \hat{R}_{hs} = R_{hs}/R_0, \quad (93)$$

where P_0, R_0 are the hot-spot pressure and radius at the beginning of the deceleration phase, and

$$\rho_* = 0.47\, m_i \left(\kappa_0 \frac{P_0^{5/2} \hat{\varepsilon}_0^{27/4}}{R_0 V_{imp}}\right)^{2/7}, \quad (94)$$

where $\hat{\varepsilon}_0$ is defined in Eq. (40). The dimensionless form of the density evolution equation becomes

$$\frac{d\hat{\rho}}{d\tau} + \frac{3\hat{\rho}}{\hat{R}_{hs}} \frac{d\hat{R}_{hs}}{d\tau} = \left(\frac{\hat{P}}{\hat{\rho}}\right)^{5/2} \frac{1}{\hat{R}_{hs}^2} \frac{1}{\hat{\varepsilon}_0^{27/4}}, \quad (95)$$

which can be numerically solved once the hot-spot radius and pressure have been determined by solving the set of Eqs. (58)–(61). The central hot-spot temperature follows from Eq. (24) of Ref. 8. A straightforward manipulation yields

$$T_{hs}(0,t) = 8.3\,(\text{keV}) \left(\frac{\Upsilon_\alpha}{2.6}\right)^{2/7} \left(\frac{V_{imp}(\text{cm/s})}{3 \times 10^7}\right)^{4/7} \frac{\hat{P}}{\hat{\rho}\hat{\varepsilon}_0^{5/2}}, \quad (96)$$

where Υ_α is defined in Eq. (40). The hot-spot areal density can also be determined by using Eqs. (23) of Ref. 8 and the definition of $\hat{\rho}$, leading to the following expression:

$$\rho R = 0.18\,(\text{g/cm}^2) \left(\frac{\Upsilon_\alpha}{2.6}\right)^{5/7} \left[\frac{V_{imp}(\text{cm/s})}{3 \times 10^7}\right]^{3/7} \hat{\rho}\hat{R}_{hs}\sqrt{\hat{\varepsilon}_0}. \quad (97)$$

To determine the stagnation value of the areal density, Eq. (95) is numerically solved using the radius and pressure of the marginally igniting shells $\hat{\varepsilon}_0 \to \infty$ discussed earlier [Eqs. (64)]. Since the hot-spot density at the beginning of the deceleration phase is negligible, we solve Eq. (95) with the initial condition $\hat{\rho}(0) \to 0$ leading to the stagnation value $\hat{\rho}_{stag} \simeq 0.83$. Substituting the marginal ignition condition $\Upsilon_\alpha \simeq 2.6$ and $\hat{R}_{stag} \simeq 1.23/\sqrt{\hat{\varepsilon}_0}$ into Eqs. (96) and (97) yields the stagnation value of the hot-spot areal density and central temperature of marginally igniting capsules:

$$\rho R(\text{stag}) = 0.18\,(\text{g/cm}^2) \left[\frac{V_{imp}(\text{cm/s})}{3 \times 10^7}\right]^{3/7}, \quad (98)$$

$$T_{hs}(r=0,\text{stag}) = 10\,(\text{keV}) \left[\frac{V_{imp}(\text{cm/s})}{3 \times 10^7}\right]^{4/7}. \quad (99)$$

To estimate the fraction θ_α of absorbed alpha particles we follow the work of Basko and set $\theta_\alpha = \text{Min}[1,\theta_0]$, where $\theta_0 \simeq 50 \int_0^{R_{hs}} \left(\rho/T_{hs}^{1.2}\right) dr$ with T_{hs} in keV and ρ in g/cm^2. After a straightforward manipulation, we find that for marginally igniting capsules (i.e., $\Upsilon_\alpha \simeq 2.6$),

$$\theta_\alpha \simeq \text{Min}\left\{1, 1.4\left[\frac{3 \times 10^7}{V_{imp}(\text{cm/s})}\right]^{9/35}\right\}, \quad (100)$$

indicating that the fraction of absorbed alpha particles is close to unity for implosion velocities typical of direct-drive ICF. If

we require that $\theta > 0.7$ for the theory to be applicable with a reasonably small error, then Eq. (100) provides a constraint on the implosion velocity, i.e., $V_{imp} < 4 \times 10^8$ (cm/s). The next step is to determine the volume average temperature to verify the assumption concerning the quadratic behavior of $\langle \sigma v \rangle$. Integrating Eq. (41) of Ref. 8 over the hot-spot volume yields $\overline{T}_{hs} \simeq 0.7 T_{hs}(0,t)$. The average temperature of marginal igniting capsules is then found from Eq. (99), and the resulting condition $\overline{T}_{hs} > 6$ keV leads to another constraint on the implosion velocity, i.e, $V_{imp} > 2 \times 10^7$ (cm/s). In summary, both assumptions are simultaneously satisfied as long as the implosion velocity is in the range

$$2 \times 10^7 < V_{imp}(\text{cm/s}) < 4 \times 10^8, \tag{101}$$

which is the typical range of directly driven capsules. Observe that the condition $\overline{T}_{hs} > 6$ keV also implies that the alpha heating is significantly larger than the radiation losses, indicating that the bremmstrahlung term can indeed be neglected in the energy equation.

Conclusions

A model for the deceleration phase and marginal ignition of imploding capsules is derived by solving a set of ordinary differential equations describing the hot-spot energy balance and the shell dynamics including the return shock propagation. The change of adiabat induced by the shock is also calculated, and the relation between the in-flight and stagnation adiabats is in general agreement with the numerical fit of *LASNEX* simulations[5] and the self-similar solution of Ref. 6. The minimum kinetic energy required for ignition is also calculated from the same model. The marginal ignition scaling is determined in terms of the stagnation as well as the in-flight adiabat. Both scaling relations are in good agreement with the numerical fit of Ref. 5.

REFERENCES

1. W. K. Levedahl and J. D. Lindl, Nucl. Fusion **37**, 165 (1997).

2. A. R. Piriz, Fusion Eng. Des. **32-33**, 561 (1996).

3. M. M. Basko, Nucl. Fusion **35**, 87 (1995).

4. M. M. Basko and J. Johner, Nucl. Fusion **38**, 1779 (1998).

5. M. C. Herrmann, M. Tabak, and J. D. Lindl, Nucl. Fusion **41**, 99 (2001).

6. A. Kemp, J. Meyer-ter-Vehn, and S. Atzeni, Phys. Rev. Lett. **86**, 3336 (2001).

7. J. Meyer-ter-Vehn, Nucl. Fusion **22**, 561 (1982).

8. Laboratory for Laser Energetics LLE Review **85**, 1, NTIS document No. DOE/SF/19460-378 (2001). Copies may be obtained from the National Technical Information Service, Springfield, VA 22161.

9. H.-S. Bosch and G. M. Hale, Nucl. Fusion **32**, 611 (1992).